

THE [N II] KINEMATICS OF R AQUARI

1983  
J. M. Hollis

1983

J. M. Hollis

Earth and Space Data Computing Division, Code 930  
NASA/Goddard Space Flight Center, Greenbelt, MD 20771

S. N. Vogel

Department of Astronomy  
University of Maryland, College Park, MD 20742

D. Van Buren

Infrared Processing and Analysis Center, Mail Stop 130-33  
California Institute of Technology, Pasadena, CA 91125

J. P. Strong

Earth and Space Data Computing Division, Code 930  
NASA/Goddard Space Flight Center, Greenbelt, MD 20771

R. G. Lyon

University of Maryland  
Center of Excellence in Space Data and Information Sciences, Code 930.5  
NASA/Goddard Space Flight Center, Greenbelt, MD 20771

and

J. E. Dorband

Applied Information Sciences Branch, Code 935  
NASA/Goddard Space Flight Center, Greenbelt, MD 20771

## ABSTRACT

We report a kinematic study of the symbiotic star system R Aqr derived from [N II]  $\lambda$  6584 emission observations with a Fabry-Perot imaging spectrometer. The [N II] spatial structure of the R Aqr jet, first observed circa 1977, and surrounding hourglass-shaped nebulosity, due to an explosion  $\sim$ 660 years ago, are derived from 41 velocity planes spaced at  $\sim$ 12 km s $^{-1}$  intervals. Fabry-Perot imagery shows the elliptical nebulosity comprising the waist of the hourglass shell is consistent with a circular ring expanding radially at 55 km s $^{-1}$  as seen at an inclination angle,  $i \sim 70^\circ$ . Fabry-Perot imagery shows the two-sided R Aqr jet is collimated flow in opposite directions. The intensity-velocity structure of the strong NE jet component is shown in contrast to the amorphous SW jet component. We offer a idealized schematic model for the R Aqr jet motion which results in a small-scale helical structure forming around a larger-scale helical path. The implications of such a jet model are discussed. We present a movie showing a side-by-side comparison of the spatial structure of the model and the data as a function of the 41 velocity planes.

## 1. INTRODUCTION

R Aqr is a symbiotic binary system with a jet embedded in complex surrounding nebulosity. In particular, the jet is presently in a period of evolution and temporal change that can only be classified as spectacular. If the system were truly understood, many fundamental questions in astrophysics would be answered.

The R Aqr binary system is comprised of a light-dominant, mass-losing,  $\sim 1.75 M_{\odot}$ , 387-day long period variable (LPV) and an unseen  $\sim 1.0 M_{\odot}$  hot subdwarf companion (see Hollis, Pedelty, & Lyon 1997 for mass justifications). The binary orbit is suspected to be highly elliptical with estimates of eccentricity ranging from  $e > 0.6$  to  $e > 0.80$  (cf. Hinkle et al. 1989; Kafatos & Michalitsianos 1982), and the binary period may be as long as  $\sim 44$  years (Willson, Garnavich & Mattei 1981; Wallerstein 1986; Hinkle et al. 1989). Due to LPV mass loss, an accretion disk is suspected to have formed around the hot companion. The accretion process would be enhanced at periastron when Roche lobe overflow occurs. The accretion disk is suspected to give rise to the symmetrical jet extensively observed at ultraviolet, optical, and radio wavelengths (e.g., see Hollis et al. 1991, Solf & Ulrich 1985, and Hollis et al. 1985, respectively, and references therein). On an observational timescale of just a few years, proper motion studies on the evolution of prominent jet features in the radio (Lehto & Johnson 1992; Hollis & Michalitsianos 1993) and ultraviolet (Hollis et al. 1997) suggest an age of  $\sim 100$  years for the R Aqr jet. Moreover, ultraviolet multi-epoch observations with HST show mass motions of the gas in the inner  $5''$  of the NE jet with tangential velocities that range from 36 to  $235 \text{ km s}^{-1}$  (Hollis et al. 1997). At a distance of 250 pc (Whitelock 1987), the components of the binary system subtend  $\sim 55$  milli-arc seconds (Hollis, Pedelty, & Lyon 1977), and, therefore, the LPV position is used as a reference point when discussing observations of the jet and surrounding nebulosity. The jet protrudes symmetrically (NE-SW) from the LPV position on a scale of a few tens of arc seconds. The jet is embedded within large-scale nebulosity which is point-

symmetric with the LPV and usually described as an elliptical nebula which is elongated 2' in right ascension.

Unfortunately, we only see the R Aqr jet and nebular structures in projection on the 2-d surface of the sky. However, the third dimension can, in principle, be inferred from radial velocity data if suitable models can be applied. Hence, Fabry-Perot spectrometers provide the high spatial and spectral resolution data to constrain potential 3-d models. For 3-d model construction it is necessary to transform calibrated intensity Fabry-Perot data cubes, which are a function of velocity, right ascension, and declination, to intensity in physical space. That is, we desire the transform:  $I(\alpha, \delta, v) \rightarrow I_{\text{model}}(x, y, z)$ . The first step assumes a value for the distance to the object, and permits the transformation of angular coordinates  $\alpha, \delta$  to linear coordinates  $x, y$ . The final step converts a radial velocity coordinate to the linear coordinate  $z$  using the constraints of a plausible model. Alternatively, in practice, one can transform a candidate  $I_{\text{model}}(x, y, z)$  into an idealized Fabry-Perot data cube  $I_{\text{model}}(\alpha, \delta, v)$  for comparison with an actual observed Fabry-Perot data cube  $I(\alpha, \delta, v)$ , and this is what we have attempted in this work.

## 2. OBSERVATIONS

R Aqr was observed with the Maryland-Caltech wide-field Fabry-Perot camera (Vogel et al. 1991) at the f8.75 Cassegrain focus of the Palomar 1.5 m telescope<sup>1</sup> on 1995

---

<sup>1</sup>The Palomar 1.5 m telescope is operated jointly by the California Institute of Technology and the Carnegie Institute of Washington.

---

September 2 with an order-isolating [N II] filter with a FWHM of 18 Å centered at 6584.7 Å. Monochromatic images and velocity fields of R Aqr were subsequently derived from these [N II]  $\lambda$  6584 observations. The camera has a 16' field of view, and employed a Tektronix 1024 x 1024 CCD which yields a scale of 0.9465" per pixel. The Fabry-Perot

etalon has an optical gap of  $\sim 200$   $\mu\text{m}$  and a finesse of 20. At a wavelength of 6584  $\text{\AA}$ , this gives a free-spectral-range (order spacing) of  $\sim 500$   $\text{km s}^{-1}$  (11  $\text{\AA}$ ) and a resolution of 25  $\text{km s}^{-1}$ .

Because of the extended nature of R Aqr and the variation in wavelength transmitted as a function of angle from the etalon optical axis, it was necessary to vary the etalon gap over a full free-spectral-range, obtaining a series of exposures at different values of the etalon gap. Nyquist sampling of the instrumental profile at [N II]  $\lambda$  6584 requires 41 exposures over the free spectral range. The wavelength transmitted as a function of position with respect to the etalon axis and the etalon optical gap was obtained by observing a hydrogen lamp at the full range of etalon spacings. Variations in the wavelength calibration were monitored and corrected during the night by observing the hydrogen lamp at a fixed etalon spacing at intervals of typically 30 minutes; the accuracy of the resulting calibration was checked using night sky lines in the object frames. The accuracy of the velocity calibration is estimated to be 2  $\text{km s}^{-1}$  rms.

The frames were bias subtracted, flat fielded, and corrected for cosmic rays. Since the center of the CCD frame varies with respect to the guide camera by a few arc seconds during the night, the frames were registered to a common grid. Then, using the calibration of wavelength transmitted as a function of position and etalon gap, the data were interpolated in velocity to produce a data cube with monochromatic planes, spaced by 0.264  $\text{\AA}$  or, equivalently, 12.03  $\text{km s}^{-1}$  for [N II]. The cubes with monochromatic planes were used for all subsequent analyses.

The right panel of Figure 1 shows spatial structure of the [N II] emission intensity of R Aqr at all velocities obtained from integrating over the main part of the line in the Fabry-Perot data cube; in this panel the strongest [N II] emission intensity is red while the weakest is blue. Representative [N II] spectra were extracted from the cube at various positions. The observed spectra are quite complex often with multiple components whose individual widths range from close to instrumental resolution to a couple of hundred  $\text{km s}^{-1}$ .

1. Despite this spectral complexity, it is illustrative to calculate the intensity-weighted mean radial velocity at each pixel and these radial velocity variations are shown within the nebula and embedded jet structures in Figure 2. Comparing Figures 1 and 2, it can be seen that the northern portion of the expanding ring and the SW jet are receding from the observer, while the southern portion of the expanding ring and the NE jet tend to approach the observer.

Figure 3 renders the observed Fabry-Perot data cube as two color-coded isosurfaces with the outer surface transparent and the interior surface totally opaque; the isosurfaces are illuminated with a light source from above. The transparent isosurface was chosen with high enough signal-to-noise value to insure that noise would not hinder discerning the morphology of the weaker elliptical nebulosity. Figure 3 upper panel is oriented such that the celestial coordinate axes ( $\alpha, \delta$ ) lie in the plane of the figure with the velocity coordinate axis implicitly perpendicular to the plane of the figure. This is the usual 'radial velocity' orientation presented to an observer or an instrument, and note that no velocity information is possible in this view of the data cube. In the figure, the central NE-SW jet is vertically aligned, and the continuum emission from the LPV is not rendered, appearing as a circular hole in the data between the NE and SW jet components. Figure 3 lower panel is slightly rotated to simultaneously view the velocity and spatial structure of both jet components and the elliptical nebulosity.

In Figure 4, the observed Fabry-Perot data cube is rendered as four color-coded isosurfaces with transparency decreasing from the outer most surface to the totally opaque interior surface. In this figure, the weaker elliptical nebulosity has not been rendered so that the velocity structure of the jet components can be more clearly seen with a horizontal velocity axis, whose extent is  $480 \text{ km s}^{-1}$ , and a vertical spatial axis, whose direction is NE-SW on the sky (i.e., NE up).

### 3. RESULTS AND DISCUSSION

Until now, the definitive kinematical study of the R Aqr nebular emission was based on long-slit spectroscopy in several red emission lines (most notably [N II]  $\lambda$  6584) obtained in 1982-1983 by Solf & Ulrich (1985). Solf & Ulrich concluded that the nebula consists of two expanding, hour-glass shells with a common axis.

The outer structure does, in fact, look like a truncated hour-glass seen in projection with a prominent equatorial waist region and fainter nebulosity that falls off rapidly above and below the waist. The spatial morphology of the waist region is elliptical, elongated 2' in right ascension, and indicates a basic plane of symmetry which has been suggested to be identical with the orbital plane of the binary system (Solf & Ulrich 1985). The waist region has an axial ratio of 3:1, and, if the material in the true plane has circular symmetry, this suggests that the orbital plane is inclined by  $\sim 20^\circ$  with respect to the line of sight along the approximate N-S direction (i.e., an inclination angle,  $i \sim 70^\circ$ ). In fact, the long-slit spectroscopy of the elliptical nebulosity is consistent with a circular ring expanding at 55  $\text{km s}^{-1}$  as seen at  $i \sim 72^\circ$  (Solf & Ulrich 1985). As reckoned from the current epoch, the outer hourglass probably represents an ejection event that occurred 660 yr ago (cf. Baade 1943, 1944).

Solf & Ulrich (1985) attribute an hour-glass morphology to the inner nebula which is elongated 1' in declination and centered within the outer nebula. However, this simple morphological description and, more importantly, the interpretation of dynamical activity of the inner nebula is complicated by an embedded, evolving, symmetrical jet that is clearly influencing the ambient medium. For example, Hollis et al. (1998) have shown that the compact inner nebulosity has undergone progressive morphological change from 1922 to 1946 which is consistent with the unexpected rise of the NE jet which was first observed above the background of the large-scale optical nebulosity circa 1977 (Wallerstein & Greenstein 1980; Herbig 1980). In 1988, the true extent of the optical R Aqr jet was realized in a novel ground-based observation which imaged the symmetrical NE-SW jet in

the light of [O III]  $\lambda$  5007 by using a vignetting disk affixed to a CCD window to reduce the light of the LPV (Hollis, Wagner, & Oliversen 1990); these optical observations showed that the symmetrical (strong NE, weak SW) jet rivals the surrounding nebulosity in scale size. As reckoned from the current epoch, an inner hourglass structure, if such there be, would represent an ejection event that occurred 200 yr ago (Solf & Ulrich 1985). On the other hand, radio proper motion studies of the NE R Aqr jet suggest an age of  $\sim$ 100 years (Lehto & Johnson 1992; Hollis & Michalitsianos 1993). It may well be that the inner nebulosity and the jet are manifestations of the same phenomenon, and that the ambient material surrounding the jet is simply relic material left behind the expanding outer nebulosity.

Since Fabry-Perot spectroscopy subsumes the capability of long-slit spectroscopy, we can easily explore whether the expanding double hour-glass model offered by Solf & Ulrich (1985) is validated in the context of constraints imposed by our Fabry-Perot data. In the case of the outer hourglass, Fabry-Perot data show both the morphology and the velocity necessary for such an interpretation. For example, Figure 3 velocity data confirms the interpretation from long-slit spectroscopy data that this weak elliptical nebulosity is consistent with a circular ring, expanding at  $55 \text{ km s}^{-1}$  as seen at  $i \sim 72^\circ$ , which represents the hourglass waist (Solf & Ulrich 1985). Moreover, Figure 1 data at all velocities confirms the truncated hourglass morphology for the outer nebula; note the extension of the hourglass walls above and below the elliptical waist, particularly at the E-W extremities. Thus, we conclude that the outer nebula in [N II]  $\lambda$  6584 is consistent with an expanding hourglass shell from both the long-slit spectroscopy (Solf & Ulrich 1985) and the Fabry-Perot data cube in this work.

Next we explore the case for an expanding inner hourglass reported by Solf & Ulrich (1985). In that context, it is illustrative to consult Figure 10 of Solf & Ulrich (1985) where the double hourglass schematic model is superimposed on a red photograph of the R Aqr nebula which looks much like the data in Figure 1 of this work. In Figure 10 of Solf &

Ulrich (1985), the putative inner hourglass structure is clearly overpowered by a NE-SW structure. Moreover, in our Figures 3 and 4, the velocity structure of the inner region of the R Aqr nebula looks nothing like the outer region, and can most simply be interpreted as dominated by a symmetrical jet. In particular, the Fabry-Perot imagery in Figure 4 shows the two-sided R Aqr jet is collimated flow in opposite directions with a much stronger intensity-velocity structure for NE jet component in contrast to the weak amorphous SW jet component. There is nothing inconsistent between our Fabry-Perot observations and the long-slit spectroscopy of Solf and Ulrich (1985), and, in fact, when we constrain our Fabry-Perot data to yield the same position-velocity diagrams as Solf and Ulrich (1985, Fig. 3a), the two look remarkably similar. However, the Fabry-Perot data afford a more complete picture (i.e., an infinitude of position angles) than a limited number of long-slit spectra would afford as regards potential jet and nebular structure geometries. Thus, we conclude that the inner nebula in [N II]  $\lambda$  6584 is not consistent with an expanding hourglass shell since the Fabry-Perot data cube clearly suggests symmetrical jet motion in the region of interest. Moreover, an animation of the Fabry-Perot cube (see Figure 1 caption) showing the observed [N II] spatial structure as a function of 41 velocity planes spaced at 12 km s<sup>-1</sup> intervals, suggests a more complicated inner region motion which results in a small-scale helical structure forming around a larger-scale helical path -- a model which we will subsequently explore.

There is theoretical and observational support for such a superimposed helical model for the jet. For example, one possible theoretical explanation for the small-scale jet structure is the following process: the ejected dust and gas is emitted along the rotation axis of the massive rotating star-accretion disk system which anchors a magnetic field; because the magnetic field is frozen into the ejected material as well as the central source, the field is twisted into a helix and the consequent increase in the azimuthal component of the magnetic field builds up a strong magnetic pressure behind the ejected material and accelerates it along the jet (Koupelis & Van Horn 1988); hence, this theory predicts an "acceleration

"region" accompanied by helical structure. In support of this theory, both Lehto & Johnson (1992) and Hollis & Michalitsianos (1993) have determined acceleration parameters for the radio R Aqr jet. More recently, Hollis et al. (1997) show that characteristic helical structures exist in the ultraviolet imagery of the R Aqr jet. The large-scale structure of the jet may simply be due to precession of the accretion disk as suggested by Hollis & Michalitsianos (1993). Next we outline our modeling approach.

In the kinematic model x, y, and z are orthogonal spatial coordinates. The x,y plane is defined to contain the circular ring radially expanding at  $\sim 55 \text{ km s}^{-1}$  with ring material at a radius of  $\sim 60$  arc seconds. The circular ring appears elliptical, suggesting that the x,y plane is inclined by  $\sim 20^\circ$  with respect to the line of sight along (i.e., an inclination angle,  $i = 70^\circ$ ). The x,y plane also indicates a basic plane of symmetry suggested to be identical with the orbital plane of the binary system (Solf & Ulrich 1985), and we adopt that interpretation also. For convenience, we can choose the x axis to be coincident with the major axis of the elliptical nebulosity. Therefore, the x axis is seen without foreshortening in the plane of the sky. As a consequence, the y axis does not lie in the plane of the sky, and is foreshortened by a factor of  $\cos(70^\circ)$ .

For convenience, we define the bulk jet motion to be in the z direction away from the orbital (x,y) plane. This is reasonable if the accretion disk, which gives rise to the jet, lies in the orbital plane. Based on an observational justification from radio jet data (Lehto & Johnson 1992; Hollis, Pedelty, & Kafatos 1997), we assume a space velocity law of the form:

$$v = k * z^p \quad (1)$$

where k and p are constants. Thus,

$$a = dv/dt = k^2 * p * z^{(2p-1)} \quad (2)$$

We hypothesize that the R Aqr jet motion results in a small-scale helical structure due to MHD effects (e.g., Koupelis & Van Horn 1988) forming around a larger-scale helical path possibly due to precession (Hollis & Michalitsianos 1993). We adopt a simple

superposition scheme for the two helices which reside on respective opening conical surfaces: both cones share a common  $z$  axis which is the outward direction of the jet. As reckoned from any point along the  $z$  axis, the position vector of a given jet parcel is just the sum of the position vector to the precession cone and the position vector to the MHD effects cone. The bulk motion constraint in equation (1) dictates the gyration velocities required in this double helix jet model. Moreover, the maximum extent of each jet is observed to be  $\sim 45$  arc seconds. The precession cone apex angle is estimated to be  $\sim 60^\circ$  (Hollis & Michalitsianos 1993). The MHD cone apex angle is estimated to be  $\sim 16^\circ$  which can be derived from the MHD helical structures shown in HST/FOC ultraviolet data (Hollis et al. 1997).

The usual geometric transformations are now required to convert the spatial coordinates  $(x, y, z)$  and space velocity coordinates  $(v_x, v_y, v_z)$  for the R Aqr model into a data cube set of coordinates  $(x, y', v_r)$  where  $y'$  is the foreshortened  $y$  value and  $v_r$  is the radial velocity observed in the line of sight. It is emphasized that  $x$  and  $y'$  are how an observer would see the model projected onto the sky.

Finally, a rotational transformation is required to obtain the observed sky orientation of the jet relative to the elliptical ring: it is necessary to rotate the jet model relative to the ring by about 30 degrees CCW. Note that this rotational transformation would not affect the projected spatial morphology or the radial velocity values of the jet, but only the jet position in relation to the elliptical nebulosity. The necessity for this transformation implies that the accretion disk does not lie in the orbital plane, which is consistent with a precessing jet interpretation.

A synchronous animation of the model cube and the data cube yields similar features (see Figure 1 caption) when the model uses  $v \sim z^{0.6}$  and  $a \sim z^{0.2}$  (cf. Hollis, Pedelty, & Kafatos 1997). In lieu of animation, volumetric rendering of the model data cube can be effective. Figure 5 is an isosurface of the model data cube that can be compared to an actual data cube shown in Figure 3 and the spatial morphology shown in Figure 1. Jet

radial velocities are in the range  $\pm 175 \text{ km s}^{-1}$ , suggesting a maximum space velocity of  $\sim \pm 512 \text{ km s}^{-1}$  for the jet. In contrast to the actual data cube, note that the model data cube does not have noise or turbulence which would be caused by its component structures interacting with an ambient medium. Moreover, in this highly idealized model, there is a lot of parameter space to explore, and it would be wise to include other species, notably Hydrogen Balmer lines and [O III]  $\lambda 5007$ , in such an exploration.

#### 4. SUMMARY

In summary, we have presented a kinematic study of the symbiotic star system R Aqr derived from [N II]  $\lambda 6584$  emission observations with a Fabry-Perot imaging spectrometer. The observed [N II] spatial structure of the R Aqr jet, first observed circa 1977, and surrounding hourglass-shaped nebulosity, due to an explosion  $\sim 660$  years ago, derive from 41 velocity planes spaced at  $12 \text{ km s}^{-1}$  intervals. The Fabry-Perot imagery shows the elliptical nebulosity comprising the waist of the hourglass shell is consistent with a circular ring expanding radially at  $55 \text{ km s}^{-1}$  as seen at an inclination angle,  $i \sim 70^\circ$  as originally reported by Solf & Ulrich (1985). On the other hand, we could not confirm the double hourglass model of Solf & Ulrich (1985) who based their analysis and interpretation on more limited long-slit spectroscopy of [N II]  $\lambda 6584$ . We suggest that the inner hourglass interpretation may have been mistaken or, at the least, confused by an evolving jet first reported circa 1977. Our Fabry-Perot imagery shows unambiguously that the two-sided R Aqr jet is collimated flow in opposite directions. The intensity-velocity structure of the strong NE jet component is shown in contrast to the amorphous SW jet component. We offer a highly idealized model for the R Aqr jet motion which results in a small-scale helical structure, which is due to magneto hydrodynamic effects (Koupelis & Van Horn 1988), forming around a larger-scale helical path, which is possibly due to precession. Moreover, we present a movie showing side-by-side comparison of the spatial

structure of this model and the actual Fabry-Perot [N II] data as a function of the 41 velocity planes.

J.M.H. received support from NASA RTOP 344-02-03-01.

## REFERENCES

Baade, W. 1943, Ann. Report Dir. Mt. Wilson Obs. 1942-1943, p. 17

Baade, W. 1944, Ann. Report Dir. Mt. Wilson Obs. 1943-1944, p. 12

Herbig, G. 1980, IAU Circ., 3535

Hinkle, K. H., Wilson, T.D., Scharlach, W.W.G., & Fekel, F.C. 1989, AJ, 98, 1820

Hollis, J.M., Bertram, R., Wagner, R.M., & Lampland, C.O. 1998, ApJ, submitted

Hollis, J.M., Kafatos, M., Michalitsianos, A.G., & McAlister, H.A. 1985, ApJ, 289, 765

Hollis, J.M., Lyon, R.G., Dorband, J.E., & Feibelman, W.A. 1997, ApJ, 475, 231

Hollis, J.M., & Michalitsianos, A.G. 1993, ApJ, 411, 235

Hollis, J.M., Oliverson, R.J., Kafatos, M., Michalitsianos, A.G., &  
Wagner, R.M. 1991, ApJ, 377, 227

Hollis, J.M., Pedelty, J.A., & Kafatos, M. 1997, ApJ, 490, 302

Hollis, J.M., Pedelty, J.A., & Lyon, R.G. 1997, ApJ, 482, L85

Hollis, J.M., Wagner, R.M., & Oliverson, R.J. 1990, ApJ, 351, L17

Kafatos, M., & Michalitsianos, A.G. 1982, Nature, 298, 540

Koupelis, T., & Van Horn, H.M. 1988, ApJ, 324, 93

Lehto, H.J., & Johnson, D.R.H. 1992, Nature, 355, 705

Solf, J. & Ulrich, H. 1985, A&A, 148, 274

Sopka, R.J., Herbig, G., Kafatos, M. & Michalitsianos, A.G. 1982, ApJ, 258, L35

Vogel, S.N., Roth, J., Kulkarni, S.R., Hester, J., & Gruendl, R. 1991, BAAS, 23, 874

Wallerstein, G. 1986, PASP, 98, 118

Wallerstein, G., & Greenstein, J.L. 1980, PASP, 92, 275

Whitelock, P.A. 1987, PASP, 99, 573

Willson, L.A., Garnavich, P., & Mattei, J.A. 1981, Inf.. Bull. Variable Stars, No. 1961

## FIGURE CAPTIONS

Fig. 1 - A side-by-side image of R Aqr in [N II] emission and our idealized model. The right panel shows the [N II] emission spatial structure of R Aqr at all velocities obtained from integrating over the main part of the line in the Fabry-Perot data cube; in this panel emission intensity increases from blue to red, north is up, and east is left. The left panel shows the model which is velocity coded with blue approaching and red receding from the observer (cf. Fig. 2 caption). Similar to Fig. 1, the movie shows a side-by-side comparison of the spatial structure of the data and the model (details in Fig. 5 caption) as a function of the 41 velocity planes. MPEG movie (~1.06 Mbytes)

Fig. 2 - A [N II] image of R Aqr showing how the intensity-weighted mean radial velocity at each pixel varies across the nebula. The color wedge at the bottom of the image ranges from  $-90 \text{ km s}^{-1}$  (blue shift) to  $+100 \text{ km s}^{-1}$  (red shift). The approaching NE jet and the receding SW jet combine to give the characteristic "S" shape of a precessing jet. Moreover, the upper portion of the hourglass is red, but its symmetry is broken by the blue NE jet -- similarly the lower portion of the hourglass is blue, but its symmetry is broken by the red SW jet.

Fig. 3 - Two isosurfaces from the [N II] Fabry-Perot data cube. The cube data numbers (DN) represent emission intensity (see text), and achieve a maximum of 24,232 DN. Isosurface values used here are rendered as a translucent 77 DN, which outlines the elliptical nebulosity comprising the waist of the hourglass shell, and an opaque (darker) 150 DN, which shows the more intense regions of the elliptical nebulosity, the strong NE jet, and the amorphous SW jet. The upper panel shows the data cube oriented with the celestial coordinate axes ( $\alpha, \delta$ ) lying in the plane of the figure (NE up and SE left) and the velocity coordinate axis implicitly perpendicular to the plane of the figure. The lower panel

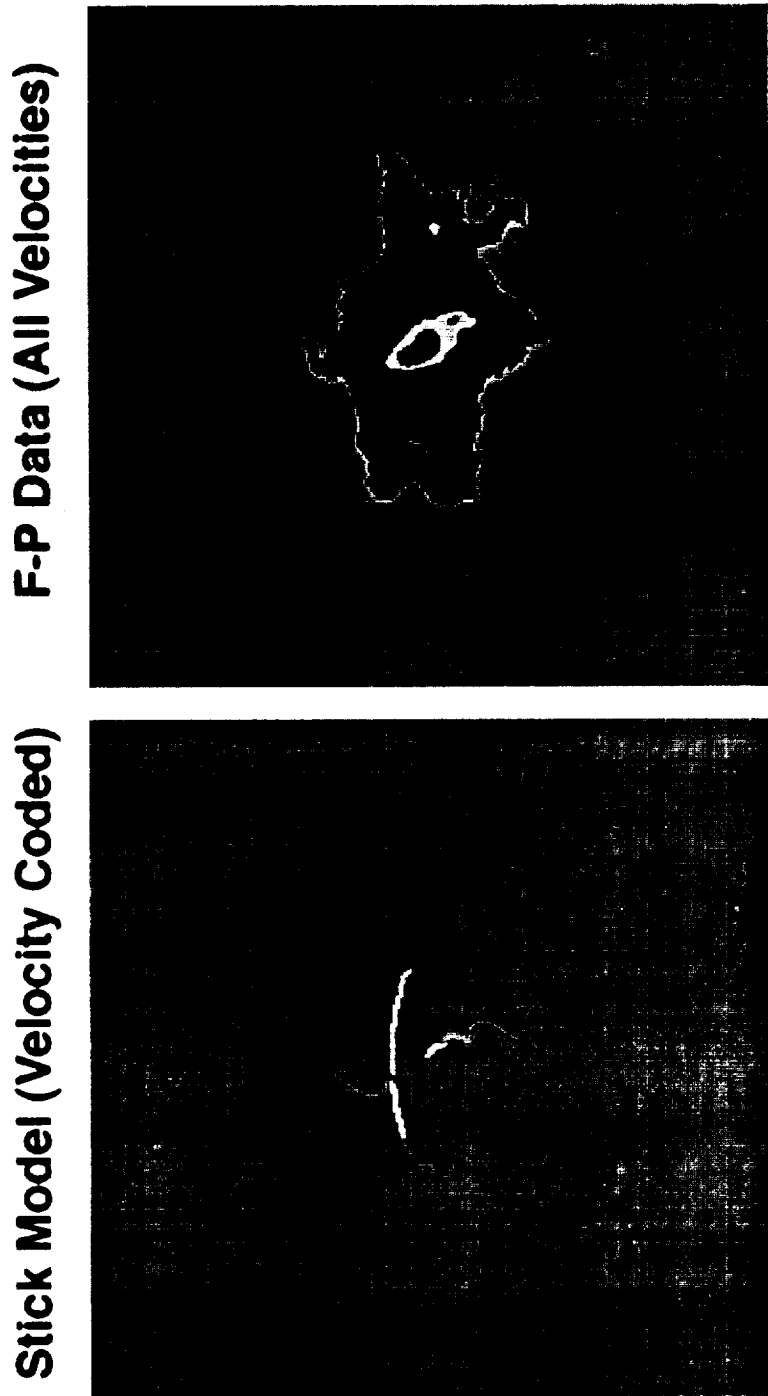
shows the data cube rotated to simultaneously view the velocity and spatial structure of both jet components; the pipe-like structure is due to continuum emission from the LPV (i.e., emission at all velocities) and is hollow since it is not rendered (cf. Fig. 4).

Fig. 4 - Four isosurfaces from the [N II] Fabry-Perot data cube. Isosurface values rendered are 150, 2400, 5000, and 20000 DN (see Fig. 3 caption) which are successively more opaque (darker). The cube is oriented so that velocity is the horizontal axis whose extent is  $480 \text{ km s}^{-1}$ . The vertical axis corresponds to the NE-SW direction on the sky (i.e., NE up). The plane of the sky is perpendicular to the plane of the figure with an observer viewing from the right. The observer sees the NE jet approaching relative to a receding SW jet. Note the intensity-velocity structure of the strong NE jet in contrast to the amorphous SW jet. The observed jet velocities here are radial and, therefore, lower limits to the true space velocities which are geometry dependent (see text).

Fig. 5 - An isosurface from a highly idealized schematic model convolved with an instrumental point spread function to simulate a data cube. This model is meant to be illustrative and not well determined, but schematically compares to the actual data cube shown in Figure 3. The upper panel shows the model data cube oriented with the celestial coordinate axes ( $\alpha, \delta$ ) lying in the plane of the figure (NE up and SE left) and the velocity coordinate axis implicitly perpendicular to the plane of the figure. The lower panel shows the model data cube rotated to simultaneously view the velocity and spatial structure of both jet components. The elliptical nebulosity is modeled as a circular ring expanding at  $55 \text{ km s}^{-1}$  as seen at an inclination angle  $i \sim 70^\circ$  (see text). The similarly inclined bipolar jet results from motion which produces a small-scale helical structure forming around a larger-scale helical path (see text for a possible explanation). In this figure, the small-scale helix has an apex angle of  $16^\circ$  which has undergone  $\sim 3.5$  turns, and the large-scale helix has an

apex angle of  $60^{\circ}$  which has undergone  $\sim 1/3$  of a turn. In this model, jet radial velocities are in the range  $\pm 175 \text{ km s}^{-1}$ , suggesting maximum jet velocities of  $\sim \pm 512 \text{ km s}^{-1}$ .

Fig. 1



Stick Model (Velocity Coded)

F-P Data (All Velocities)

### Intensity-Weighted Mean Velocity Image

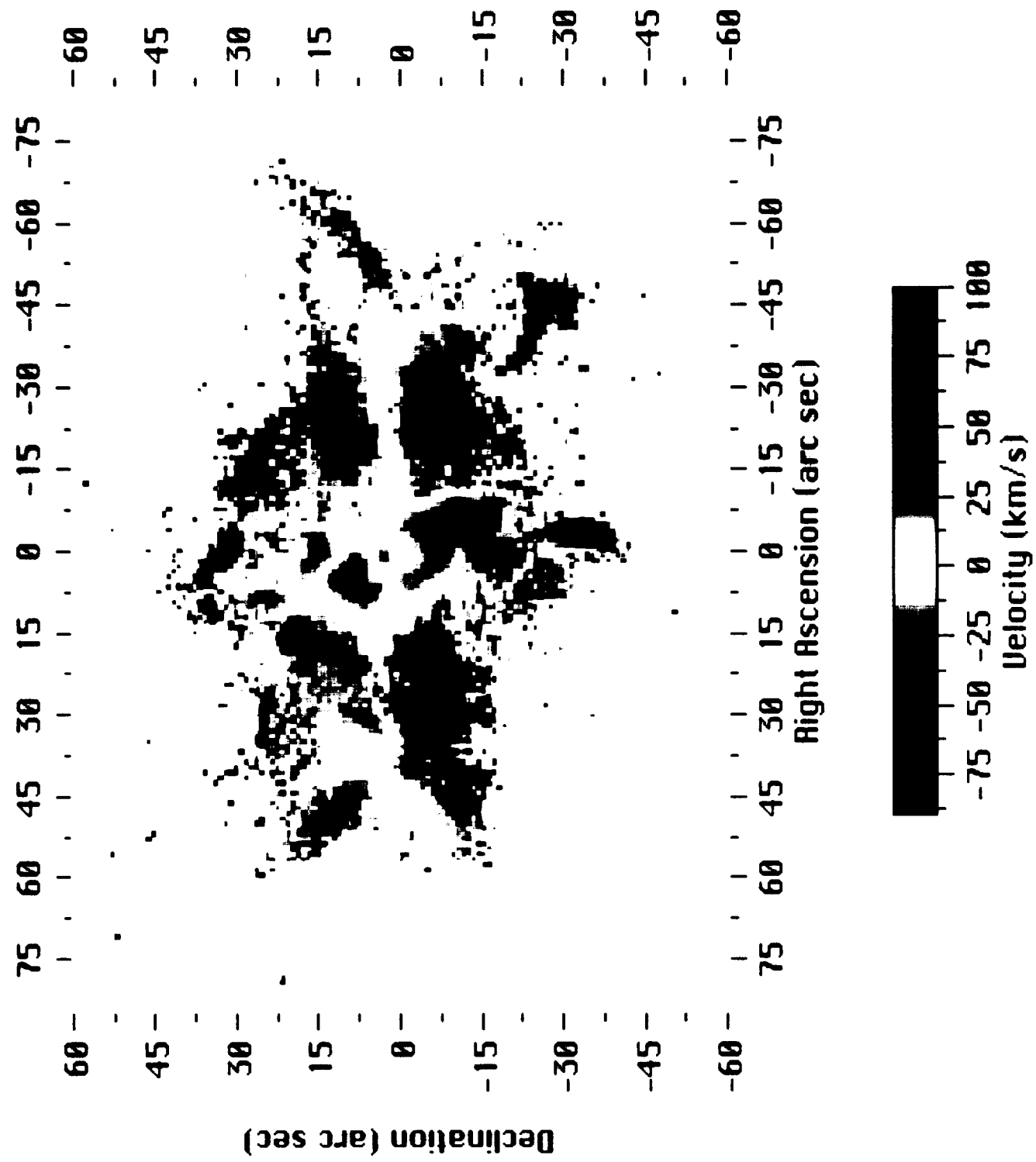


Fig. 2

Fig. 3  
(UPPER)



Fig. 3  
(lower)



Fig. 4



Fig. 5  
(UPPER)

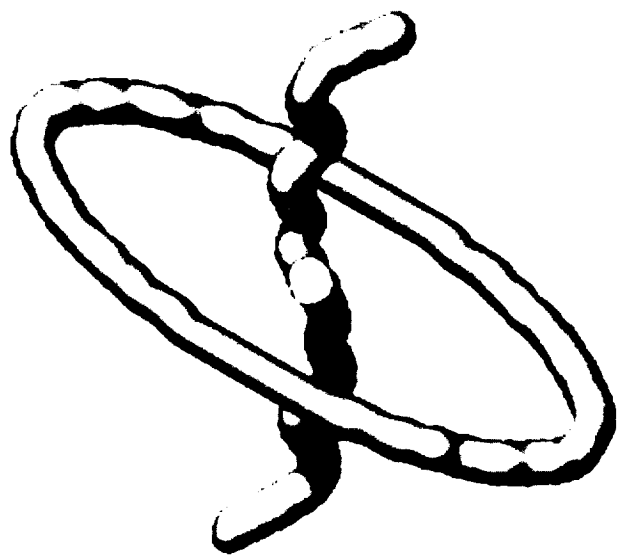


Fig. 5  
(lower)

